



# Effects of Co Substitution on the Microstructural, Infrared, and Electrical Properties of $\text{Mg}_{0.6-x}\text{Co}_x\text{Zn}_{0.4}\text{Fe}_2\text{O}_4$ Ferrites

Esam AlArfaj<sup>1</sup> · Sobhi Hcini<sup>2,3</sup> · Abdulrahman Mallah<sup>4</sup> · Mohamed Houcine Dhaou<sup>1,5</sup> · Mohamed Lamjed Bouazizi<sup>6</sup>

Received: 18 February 2018 / Accepted: 11 April 2018 / Published online: 18 April 2018  
© Springer Science+Business Media, LLC, part of Springer Nature 2018

## Abstract

Spinel ferrites having  $\text{Mg}_{0.6-x}\text{Co}_x\text{Zn}_{0.4}\text{Fe}_2\text{O}_4$  ( $0 \leq x \leq 0.6$ ) compositions were prepared using the sol–gel method. XRD patterns show that samples have the cubic phase of the spinel ferrite with the  $Fd\bar{3}m$  space group. The obtained values of the lattice constant and porosity increase with increasing cobalt concentration. FTIR spectra show only the tetrahedral stretching peaks that are shifting towards higher frequencies with increasing Co content. The substitution of Mg by Co leads to the decrease of conductivity of the samples. The behaviors of the real part of permittivity and loss tangent have been investigated using Maxwell theory. Electrical modulus and impedance results show the presence of the electrical relaxation phenomenon for the samples with non-Debye type. The Nyquist representations have been analyzed using a proposed electrical circuit, and the results show that the resistances of the prepared samples resulted mostly from the grain boundary effect.

**Keywords** Ferrites · Sol–gel method · Microstructural properties · Infrared properties · Electrical properties

## 1 Introduction

Ferrites with a spinel structure have attracted much interest in many fields particularly in modern electronic technologies. These materials are used as information storage

systems, microwave devices, computer memory chips, gas sensors, magnetic recording media, transformers, transducers, and other devices [1]. However, to widen the range of electronic applications for spinel ferrites, the improvement of their electrical properties is very necessary. In this context, impedance spectroscopy (IS) is a good technique that has been widely used to understand the electrical properties of spinel ferrites. This technique allows investigating, analyzing, and differentiating the dielectric and conduction behaviors within the chosen of frequency and temperature domains [2]. Recently, many studies have been reported and presented in the literature for different ferrite systems characterized using the IS technique [3–6]. These studies showed that the IS properties of ferrite materials are highly influenced by several factors, namely the type of substitutional elements, the amount of substitution, the sintering temperatures, chemical composition, microstructure of the material, the difference in ionic radii, grain and grain boundary effects, and the cation distribution between interstitial sites.

Among ferrites, the Mg–Zn system is considered as a favorable choice in the industry due to its uses in power transformers, microwave devices, and telecommunication [7]. In this case, various compositions have been investigated and reported in the literature for the Mg–Zn system [8–11]. However, in order to improve its practical

✉ Mohamed Houcine Dhaou  
dhaouhoucine5@gmail.com

✉ Sobhi Hcini  
hcini\_sobhi@yahoo.fr

<sup>1</sup> College of Sciences, Department of Physics, Qassim University, Buraydah Almolaydah, Buraydah, Saudi Arabia

<sup>2</sup> Research unit of valorization and optimization of exploitation of resources, Faculty of Science and Technology of Sidi Bouzid, University Campus Agricultural City, University of Kairouan, 9100 Sidi Bouzid, Tunisia

<sup>3</sup> Buraydah of Technical College at Al-Asyiah, Al-Asyiah - King Abdulaziz Road, PB: 304, Al-Asyiah 51971, Saudi Arabia

<sup>4</sup> Department of Chemistry, College of Sciences, Qassim University, Buraydah Almolaydah, P.O.Box: 6644, Buraydah, 51452 Saudi Arabia

<sup>5</sup> Laboratory of Studies of Thermal Systems and Energy, National Engineering School of Monastir, University of Monastir, Ibn Eljazzar Road, 5019 Monastir, Tunisia

<sup>6</sup> College of Engineering, Prince Sattam Bin Abdulaziz University, 655, Al Kharj 11942, Saudi Arabia

applications, many substitutions were made on Mg–Zn ferrite [12–15]. For example, the effects of Ni<sup>2+</sup> doping on structural and magnetic properties of Mg<sub>0.7</sub>Zn<sub>0.3</sub>Fe<sub>2</sub>O<sub>4</sub> ferrite have been reported by D.H. Bobade et al. [12]. For their part, M.A. Rafiq et al. have studied the structural and electromagnetic properties of Mg<sub>0.6</sub>Zn<sub>0.4</sub>Fe<sub>2</sub>O<sub>4</sub> nanocrystals with Co<sup>2+</sup> substitution [13]. In their work, B.P. Ladgaonkar et al. have studied the infrared absorption spectroscopic properties of Nd<sup>3+</sup>-substituted Zn–Mg ferrites [14]. On the other hand, a detailed study of structural, magnetic, and dielectric behaviors of Mg<sub>0.5</sub>Zn<sub>0.5</sub>Fe<sub>2</sub>O<sub>4</sub> with Cu substitution has been presented by H.M. Zaki et al. [15].

However, to the best of our knowledge, the reports on properties of Mg–Zn ferrite with specific compositions Mg<sub>0.6-x</sub>Co<sub>x</sub>Zn<sub>0.4</sub>Fe<sub>2</sub>O<sub>4</sub> ( $0 \leq x \leq 0.6$ ) are not investigated. In the present work, we have investigated the sol–gel synthesis of these ferrites, and we present successively their room temperature microstructural, infrared, and electrical properties.

## 2 Experimental Details

Ferrite samples with Mg<sub>0.6-x</sub>Co<sub>x</sub>Zn<sub>0.4</sub>Fe<sub>2</sub>O<sub>4</sub> ( $0 \leq x \leq 0.6$ ) compositions were prepared by sol–gel method using stoichiometric amounts of Mg(NO<sub>3</sub>)<sub>2</sub>·6H<sub>2</sub>O, Co(NO<sub>3</sub>)<sub>2</sub>·6H<sub>2</sub>O, ZnN<sub>2</sub>O<sub>6</sub>·H<sub>2</sub>O, and Fe(NO<sub>3</sub>)<sub>3</sub>·9H<sub>2</sub>O, all with purity better than 99.9%. The different synthesis steps of the samples are shown in Fig. 1. The synthesized ferrites are characterized at room temperature (RT) by several experimental techniques. The phase purity, structure, and cell parameters are checked using an X-ray diffractometer (Shimadzu lab 6000) with CuK<sub>α1</sub> radiation ( $\lambda = 1.5406 \text{ \AA}$ ). The data collection was performed in the range of  $10^\circ \leq 2\theta \leq 80^\circ$  with a step size of  $0.01^\circ$  and a counting time of 0.6 s. Scanning electron microscopy (SEM; Philips XL30 microscope) has been used to analyze the morphologies of the samples under an accelerating voltage of 20 kV. FTIR spectra were performed using a Shimadzu Fourier Transform Infrared Spectrophotometer (FTIR-8400S) in the wavenumber range of 400–4100 cm<sup>-1</sup> with a resolution of 1 cm<sup>-1</sup>. Frequency-dependent dielectric measurements of the present samples were evaluated at room temperature using N4L-NumetriQ (model PSM1735) connected to a computer over the frequency range of 40–10<sup>6</sup> Hz. For dielectric measurements, sintered pellets were coated with high-purity silver paste on adjacent faces as electrodes and then dried for few hours at 150 °C to make the parallel plate capacitor geometry.

The real part of permittivity  $\epsilon'$  was calculated using the following formula:

$$\epsilon' = \frac{Ct}{\epsilon_0 A} \quad (1)$$

where  $C$  represents the capacitance of the pellet,  $t$  is the thickness of the pellet,  $\epsilon_0$  is the permittivity of free space, and  $A$  is the area of the cross section of the pellet

The imaginary part of permittivity  $\epsilon''$  was calculated by the following relation:

$$\epsilon'' = \frac{\sigma}{\omega \epsilon_0} \quad (2)$$

where  $\sigma$  is the electrical conductivity and  $\omega = 2\pi f$  is the angular frequency.

The loss factor ( $\tan\delta$ ) and real ( $M'$ ) and imaginary ( $M''$ ) parts of the electric modulus are deduced from  $\epsilon'$  and  $\epsilon''$  values as follows:

$$\tan(\delta) = \frac{\epsilon''}{\epsilon'} \quad (3)$$

$$M' = \frac{\epsilon'^2}{(\epsilon'^2 + \epsilon''^2)} \quad (4)$$

$$M'' = \frac{\epsilon''^2}{(\epsilon'^2 + \epsilon''^2)} \quad (5)$$

## 3 Results and Discussion

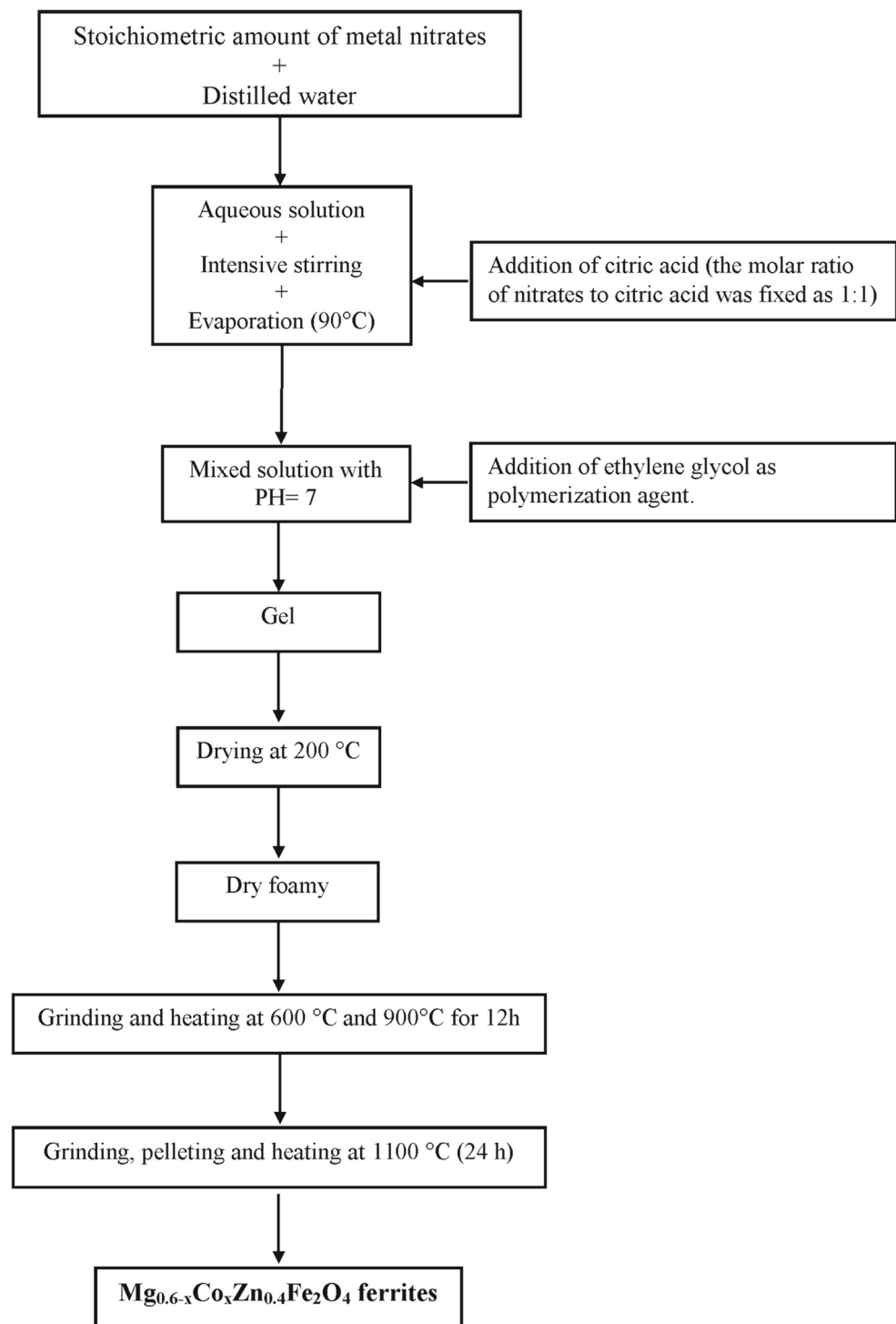
### 3.1 Microstructural Analysis

XRD patterns of Mg<sub>0.6-x</sub>Co<sub>x</sub>Zn<sub>0.4</sub>Fe<sub>2</sub>O<sub>4</sub> ( $0 \leq x \leq 0.6$ ) ferrites are shown in Fig. 2. For all samples, these patterns show the presence of the main characteristic peaks of the cubic spinel phase. The absence of additional peaks related to impurities indicates the high purity of the prepared samples. All peaks are indexed in the cubic  $Fd\bar{3}m$  symmetry using X'Pert HighScore Plus software. From the most intense peak (311), we calculated the lattice constant using the following equation [16]:

$$\lambda a = \frac{\sqrt{h^2 + l^2 + k^2}}{2 \sin\theta} \quad (6)$$

where  $\lambda$  is the wavelength,  $a$  is the lattice constant, and  $(hkl)$  are the Miller indices. We present in Table 1 the calculated  $a$  values for all samples. As observed from this table, the lattice constant increases with increasing Co content in the Mg<sub>0.6-x</sub>Co<sub>x</sub>Zn<sub>0.4</sub>Fe<sub>2</sub>O<sub>4</sub> system. This can be related to the higher ionic radius of Co<sup>2+</sup> ions (0.745 Å) compared with that of Mg<sup>2+</sup> ions (0.72 Å) [17]. A similar behavior has been observed in other cobalt-substituted magnesium ferrites [18, 19]. The variations of X-ray density ( $D_x$ ), bulk density ( $D_b$ ), and porosity ( $P$ ) are reported in Table 1 as a function

**Fig. 1** Schematic diagram representing the preparation of  $\text{Mg}_{0.6-x}\text{Co}_x\text{Zn}_{0.4}\text{Fe}_2\text{O}_4$  ferrites



of Co concentration. The X-ray density was calculated using the following equation [20]:

$$D_x = \frac{8M}{Na^3} \quad (7)$$

where  $M$  is the molecular weight,  $N$  is Avogadro's constant, and  $a$  is the lattice constant. It is clear from Table 1 that

the theoretical density ( $D_x$ ) increases with the increase of  $\text{Co}^{2+}$  content. This can be ascribed to the higher density of cobalt ( $8.9 \text{ g cm}^{-3}$ ) compared with that of magnesium ( $1.738 \text{ g cm}^{-3}$ ). The measured density was calculated using the relation [20]

$$D_b = \frac{m}{\pi r^2 h} \quad (8)$$

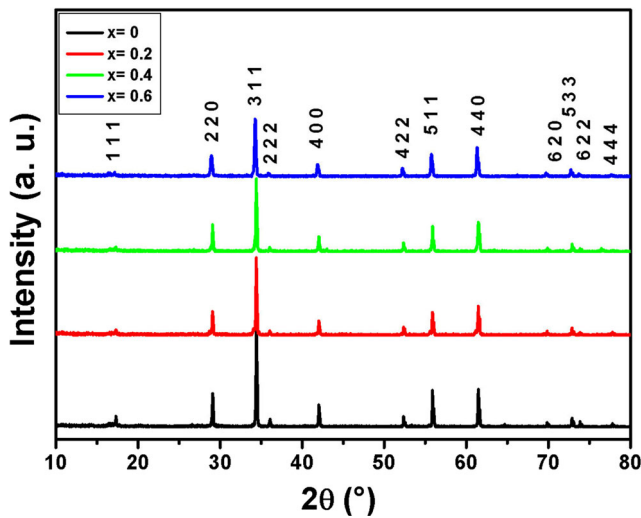


**Fig. 2** XRD patterns of  $\text{Mg}_{0.6-x}\text{Co}_x\text{Zn}_{0.4}\text{Fe}_2\text{O}_4$  ferrites. All peaks are indexed in the cubic spinel-type structure ( $Fd\bar{3}m$  space group)

where  $m$ ,  $r$ , and  $h$  represent the mass, radius, and thickness of the samples, respectively. In good agreement with  $D_x$  values, the bulk density ( $D_b$ ) shows a similar decreasing behavior with increasing Co content. The difference between both densities can be attributed to the porosity of the samples which was estimated as follows [20]:

$$P = \left(1 - \frac{D_b}{D_x}\right) \times 100 \quad (9)$$

As shown in Table 1, the present values of porosity increase with increasing Co concentration. The average crystallite size is obtained using the Scherer formula from XRD peaks as follows [21]:

$$\lambda D_{\text{XRD}} = \frac{0.9\lambda}{\beta \cos(\theta)} \quad (10)$$

where  $\lambda$  is the employed X-ray wavelength,  $\theta$  is the diffraction angle for (3 1 1) peak, and  $\beta$  its full width at half maximum

**Table 1** Structural parameters deduced from XRD data and infrared results for  $\text{Mg}_{0.6-x}\text{Co}_x\text{Zn}_{0.4}\text{Fe}_2\text{O}_4$  ferrites

Parameters	0	0.2	0.4	0.6
$a$ (Å)	8.6299	8.6345	8.6372	8.6665
$D_x$ ( $\text{g cm}^{-3}$ )	4.473	4.609	4.747	4.841
$D_b$ ( $\text{g cm}^{-3}$ )	4.338	4.452	4.511	4.547
$P$ (%)	3.018	4.406	4.972	6.073
$D_{\text{XRD}}$ (nm)	119	138	110	69
$L_A$ (Å)	3.7368	3.7388	3.7400	3.7527
$L_B$ (Å)	3.0511	3.0527	3.0537	3.0640
IR band wavelength ( $\text{cm}^{-1}$ )				
$\nu_1$ (~400)	–	–	–	–
$\nu_2$	535	536	538	540

(FWHM). The estimated values of  $D_{\text{XRD}}$  decrease with increasing Co content as shown in Table 1. Figure 3 presents the SEM images of  $\text{Mg}_{0.6-x}\text{Co}_x\text{Zn}_{0.4}\text{Fe}_2\text{O}_4$  ferrites with  $x = 0, 0.2, 0.4$ , and  $0.6$ , respectively. For all the samples, the micrographs present regular-shaped grains with spherical morphology. The estimated values of the average crystallite size decrease from  $1.339 \mu\text{m}$  (for  $x = 0$ ) to  $0.942 \mu\text{m}$  (for  $x = 0.6$ ). The images also show black spots associated to the porosity of the samples. As shown in Fig. 3, these areas increase when increasing Co content resulting in an increase of the porosity. This is in good accordance with the porosity estimated from XRD data.

### 3.2 FTIR Spectra

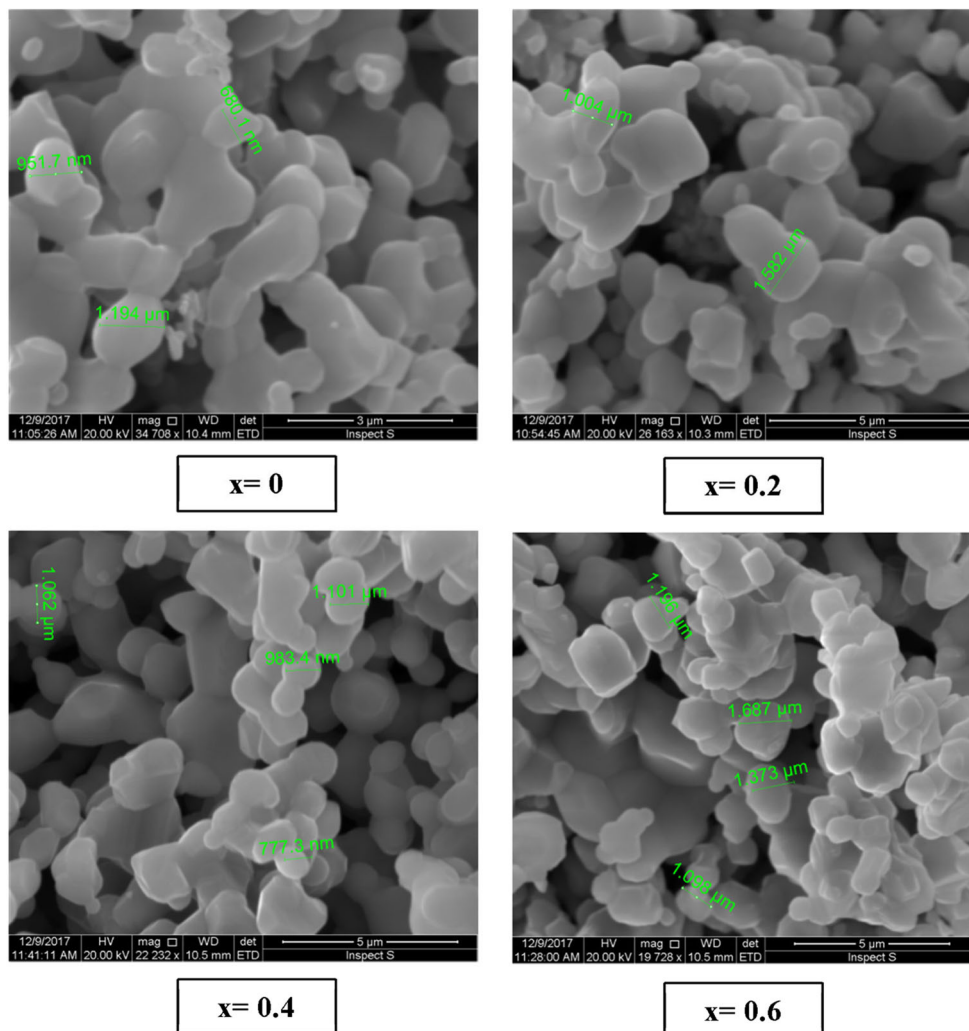
To detect the absorption bands and to ensure the formation of the spinel ferrite phase in  $\text{Mg}_{0.6-x}\text{Co}_x\text{Zn}_{0.4}\text{Fe}_2\text{O}_4$  samples, infrared spectroscopy analysis was carried out at RT in the range of  $400$  to  $4100 \text{ cm}^{-1}$  (see Fig. 4). Generally, two characteristic absorption peaks were observed in the FTIR spectra of spinel ferrites that are related to the intrinsically stretching vibrations of oxygen bands with metal cations at the A and B positions [22]. As shown from Fig. 4, two principal absorption bands are shown from these spectra. The first band observed around  $400 \text{ cm}^{-1}$  (low frequency  $\nu_1$ ) is attributed to the vibration of metal–oxygen at the octahedral site ( $\text{M}[6] \leftrightarrow \text{O}$ ), while the second band in the range of  $535$ – $540 \text{ cm}^{-1}$  (high frequency  $\nu_2$ ) corresponds to the vibration of metal–oxygen at the tetrahedral site ( $\text{M}[4] \leftrightarrow \text{O}$ ). From the spectra, only tetrahedral stretching peaks are clearly observed since octahedral stretching is near  $400 \text{ cm}^{-1}$ . The peak positions corresponding to frequency  $\nu_2$  of the studied samples are listed in Table 1. It is clear from this table that  $\nu_2$  values increase slightly from  $535$  to  $540 \text{ cm}^{-1}$  with increasing Co concentration from  $x = 0$  to  $0.6$ . This shift of the tetrahedral stretching frequency matches well with the frequencies reported in literature for cobalt-substituted magnesium ferrites [23, 24]. On the other hand, the FTIR spectra also show the presence of other negligible bands around  $1540$  and  $3740 \text{ cm}^{-1}$ . These bands are due to the bending and stretching vibration of  $\text{H}_2\text{O}$  molecules, which indicates remnants of hydroxyl groups during the sample preparation [24].

### 3.3 Electrical Properties

#### 3.3.1 Electrical Conductivity

We represent in Fig. 5 the frequency variation of the conductivity at RT for  $\text{Mg}_{0.6-x}\text{Co}_x\text{Zn}_{0.4}\text{Fe}_2\text{O}_4$  ferrites. The conductivity analysis can provide significant information related to the conduction process of these materials. In the

**Fig. 3** Scanning electron micrographs for  $Mg_{0.6-x}Co_xZn_{0.4}Fe_2O_4$  ferrites



case of ferrite materials, the conduction process is generally due to the electron hopping between  $Fe^{2+}$  and  $Fe^{3+}$  present at the octahedral site. From Fig. 5, we can observe

gradual increases of the conductivity with frequency. Indeed, the curves show a change in conduction regime at a certain frequency, called hopping frequency  $f_h \approx 10^5$  Hz. This hopping frequency moves towards high frequencies as the Co concentration increases. For the frequencies  $f < f_h$ , the conductivity is independent of the frequency and is in the form of a plateau. This frequency region corresponds to the dc conductivity ( $\sigma_{dc}$ ), which is composition dependent. The low conductive grain boundaries are more active in this frequency region; hence,  $Fe^{2+} \leftrightarrow Fe^{3+}$  electron hopping is less. For  $f > f_h$ , the conductivity is frequency depend and increases exponentially. At this frequency region, the conductive grains become more active which promotes the conduction mechanism. To verify this, we modeled the conductivity data using the following power law [25]:

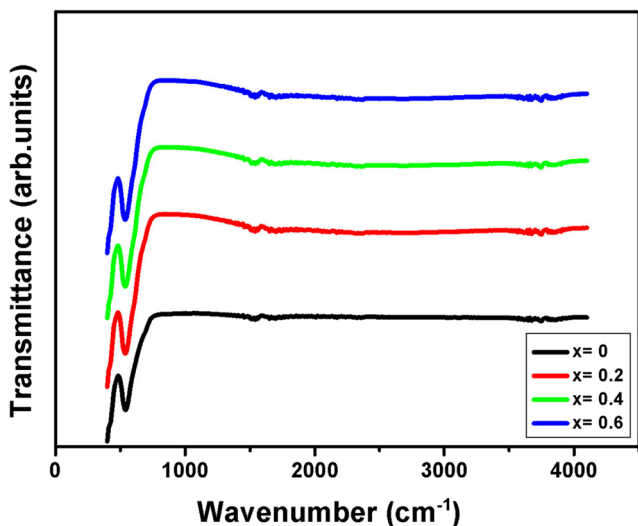


**Fig. 4** FTIR spectra of  $Mg_{0.6-x}Co_xZn_{0.4}Fe_2O_4$  ferrites recorded at RT

$$\sigma_{tot} = \sigma_{dc} + Bf^s \tag{11}$$

where  $B$  and  $s$  are the pre-exponential and exponent factors, respectively. The value of  $s$  ranges between 0 and 1 [26]. The modeling of experimental curves using (11) shows a good agreement between the theoretical and experimental

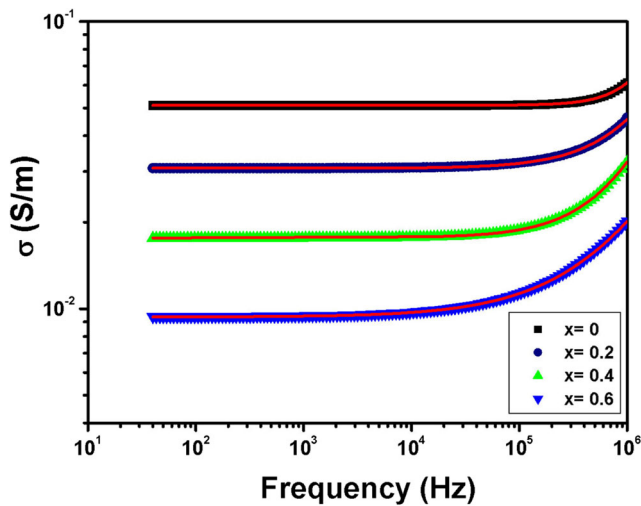


**Fig. 5** Variation of conductivity vs. frequency at RT for  $\text{Mg}_{0.6-x}\text{Co}_x\text{Zn}_{0.4}\text{Fe}_2\text{O}_4$  ferrites. Red solid lines represent the fitting to the experimental data using the universal Jonscher power law

curves of the studied samples (see Fig. 5). The fitting parameters are given in Table 2. This table shows that the value of the  $s$  exponent ranges between 0.667 and 0.942, which indicates that the conduction process in the samples follows the localized electron hopping model. The results also show a decrease of both dc conductivity and  $s$  exponent with Co substitution. This indicates that the electron hopping decreases with the addition of Co in  $\text{Mg}_{0.6-x}\text{Co}_x\text{Zn}_{0.4}\text{Fe}_2\text{O}_4$  ferrites. A similar decrease in conductivity has been observed in other cobalt-substituted magnesium ferrites [20, 27]. Our result can be confirmed by considering the jump length ( $L$ ) of the charge carriers. The jump lengths of the A and B sites are determined from the relations given as [28]

$$L_A = a \left( \frac{\sqrt{3}}{4} \right) \quad (12)$$

and

$$L_B = a \left( \frac{\sqrt{2}}{4} \right) \quad (13)$$

**Table 2** Fitting parameters using Jonscher power law obtained from the experimental data of conductivity as a function of frequency at RT for  $\text{Mg}_{0.6-x}\text{Co}_x\text{Zn}_{0.4}\text{Fe}_2\text{O}_4$  ferrites

Co content ( $x$ )	$\sigma_{\text{dc}} \times 10^{-2}$ (S/m)	$B \times 10^{-8}$	$s$	$\chi^2$
0	4.973	4.33	0.942	0.995
0.2	3.093	7.35	0.881	0.999
0.4	1.707	81.90	0.706	0.997
0.6	0.936	94.35	0.667	0.998

where  $a$  is the lattice constant. The calculated values of  $L_A$  and  $L_B$  are given in Table 1. It has been observed that  $L$  increases with Co doping, which suggests that charge carriers require more energy to jump from one cationic site to another. This leads to the decrease of the conductivity of the synthesized ferrites.

### 3.3.2 Real Part of Permittivity and Loss Factor

In this part, we are interested in studying the dielectric properties of  $\text{Mg}_{0.6-x}\text{Co}_x\text{Zn}_{0.4}\text{Fe}_2\text{O}_4$  ferrites by presenting the frequency variation of their real part of permittivity ( $\epsilon'$ ) and loss factor ( $\tan\delta$ ) at RT (see Fig. 6a, b). For all samples, it is observed that  $\epsilon'$  and  $\tan\delta$  values are higher at low frequencies, then they decrease monotonously and become very low at high frequency. Similar results have been observed in other studies [29–32]. The behavior of both dielectric constants can be explained by the theory of interfacial polarization predicted by Maxwell [33]. The dielectric structure of ferrite should be divided into two parts: grains with high conductivity and grain boundaries that act as insulators.

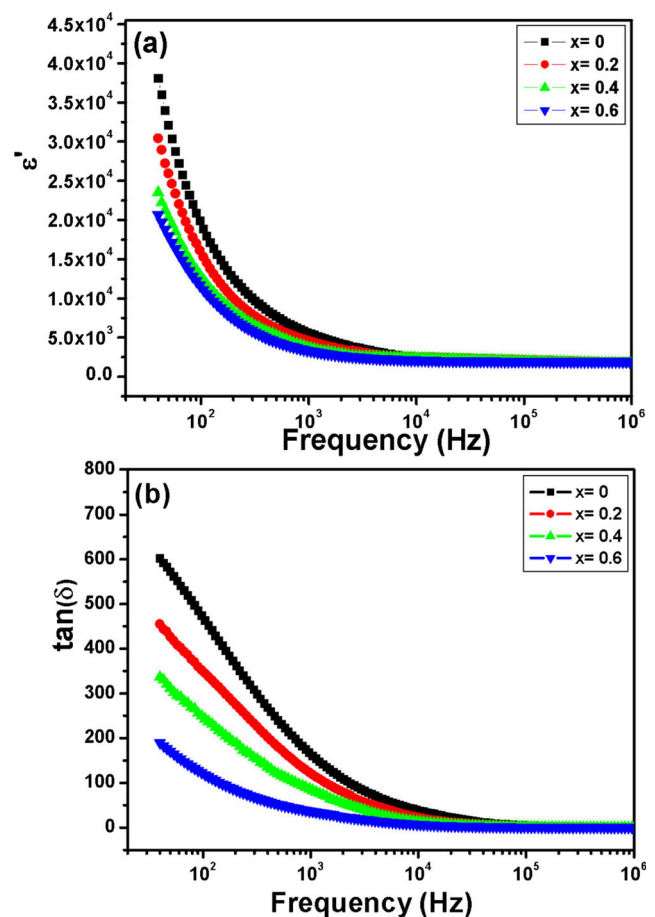


**Fig. 6** Frequency dependence at RT of the real part of permittivity (a) and loss factor (b) for  $\text{Mg}_{0.6-x}\text{Co}_x\text{Zn}_{0.4}\text{Fe}_2\text{O}_4$  ferrites

Under the influence of an electric field, the displacement of charges in the grains is interrupted at the grain boundaries. This causes the accumulation of charges at the interface, thus the appearance of an interfacial polarization. At high frequency,  $Fe^{2+} \leftrightarrow Fe^{3+}$  electron exchange does not follow the applied field, which results in a decrease in the contribution of the interfacial polarization. Consequently, the values of dielectric constants become very low at high frequency, reaching values in the order of  $10^{-1}$ . The low loss at higher frequencies identifies the potential of these ferrites for high-frequency applications [34]. At the low-frequency region, the values of the loss factor decrease with the substitution of Mg by Co in good agreement with the decrease of the conductivity.

### 3.3.3 Electrical Modulus

The variation of the real part of the electrical modulus ( $M'$ ) with frequency at RT for  $Mg_{0.6-x}Co_xZn_{0.4}Fe_2O_4$  ferrites is presented in Fig. 7a. For all samples, it is observed that  $M'$  values are very low in low frequency region, confirming that the electrode polarization makes a negligible contribution in the materials [35]. A continuous increase in  $M'$  with increasing frequency was observed, and the values tend to saturate at a maximum asymptotic value in the high-frequency region. This may be due to the short-range mobility of charge carriers [36, 37]. Figure 7b shows the curves of the imaginary component of the modulus ( $M''$ ) vs. frequency at RT for the samples. The  $M''(f)$  spectra are characterized by well-resolved peaks appearing at the characteristic frequency ( $f_{M''}^{max}$ ) for the different compositions (Fig. 7b). The positions of these peaks shift towards the lower frequency side with increasing Co content. This suggests that the relaxation process decreases with doping Mg by Co. The  $M''(f)$  data were well fitted using the Bergman proposed Kohlrausch, Williams, and Watts (KWW) function [38]:

$$M'' = M''_{max} / \left[ 1 - \beta + \left( \frac{\beta}{1 + \beta} \right) \left( \beta \left( \frac{f_{max}}{f} \right) + \left( \frac{f}{f_{max}} \right)^\beta \right) \right] \tag{14}$$

where  $M''_{max}$  is the peak maxima and  $f_{max}$  its corresponding frequency and  $\beta$  is the stretching factor ( $0 < \beta < 1$ ). This factor decides whether the relaxation in dielectric is Debye or non-Debye in nature [39]. The fitting parameters of  $M''(f)$  data using (14) are given in Table 3. The  $\beta$  values for all samples turned out to be less than unity and decrease with increasing Co content. The fact that  $\beta$  values are less than unity shows the non-Debye nature of the samples. The decrease of  $\beta$  when substituting Mg by Co is related to the decrease of the average grain size [40]. Since the

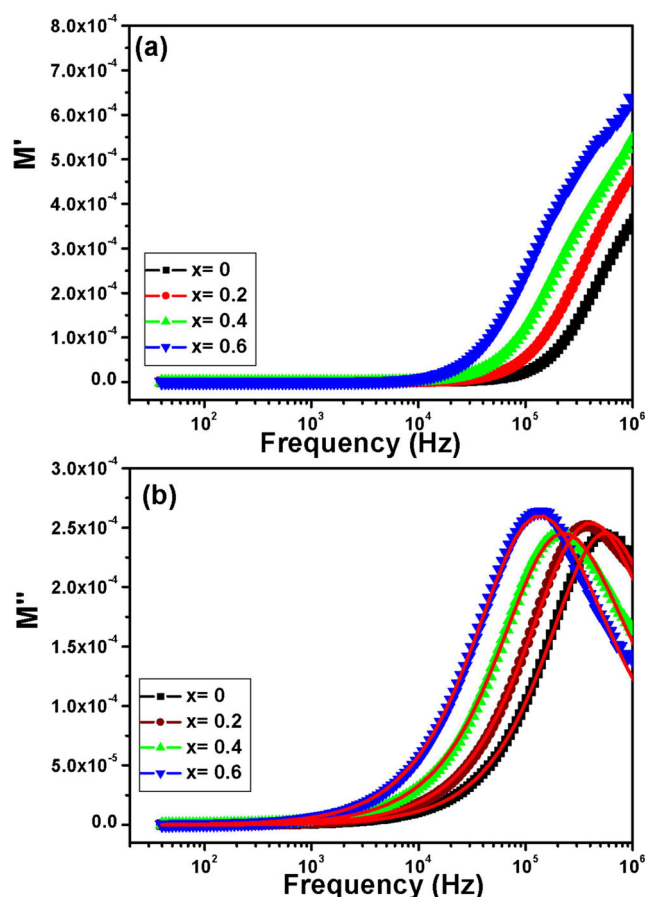


**Fig. 7** Frequency dependence at RT of real part  $M'$  (a) and imaginary part  $M''$  (b) of the electrical modulus for  $Mg_{0.6-x}Co_xZn_{0.4}Fe_2O_4$  ferrites. Red solid lines represent the fitting to the experimental data of  $M''(f)$  using (14)

grain boundary volume increases due to the reduction of the average crystallite size, the number of dipoles in the grain boundary also increases significantly. As a result, the interaction among the dipoles within the grain boundary increases and hence the dipole relaxation becomes slower, reducing the relaxation frequency ( $f_{max}$ ). This reduction in the relaxation frequency leads to the increase of the relaxation time ( $\tau_{M''}$ ) given by the following relation:

$$\tau_{M''} = 1/2\pi f_{max}, \tag{15}$$

**Table 3** Fitting parameters obtained from the experimental data of the imaginary part of the electrical modulus as a function of frequency at RT for  $Mg_{0.6-x}Co_xZn_{0.4}Fe_2O_4$  ferrites

Co content (x)	$M''_{max} (\times 10^{-4})$	$\beta$	$f_{M''}^{max}$ (Hz)	$\tau (\times 10^{-7} \text{ s})$
0	2.449	0.830	559,318	2.846
0.2	2.538	0.752	405,912	3.921
0.4	2.456	0.738	227,688	6.990
0.6	2.633	0.728	135,607	11.737

Using this equation, the obtained values of  $\tau_{M''}$  increase from  $2.846 \times 10^{-7}$  s for  $x = 0$  to  $11.737 \times 10^{-7}$  s for  $x = 0.6$ .

### 3.3.4 Electrical Impedance

The curves of the real part ( $Z'$ ) of impedance vs. frequency at RT for  $\text{Mg}_{0.6-x}\text{Co}_x\text{Zn}_{0.4}\text{Fe}_2\text{O}_4$  ferrites are presented in Fig. 8a. These curves show that  $Z'$  values decrease as the frequency increases, indicating an increase in the values of ac conductivity with frequency. These curves also reveal that  $Z'$  values increase with increasing Co content in agreement with previous conductivity results. In the higher-frequency region (above  $10^6$  Hz),  $Z'$  values are found to merge for all compositions and become independent of frequency. This behavior can be interpreted on the basis of space charge polarization. A similar variation of  $Z'$  was observed for other ferrite systems [3–6]. The RT variation of an imaginary part of impedance ( $Z''$ ) for the samples vs. frequency is shown in Fig. 8b. The values of  $Z''$  show

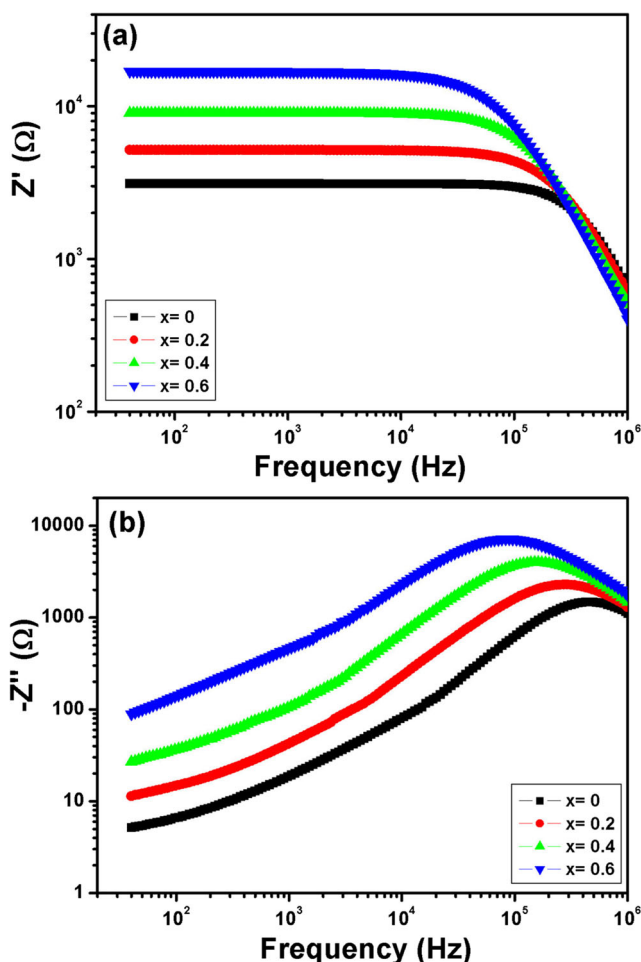


**Fig. 8** Frequency dependence at RT of real part  $Z'$  (a) and imaginary part  $Z''$  (b) of electrical impedance for  $\text{Mg}_{0.6-x}\text{Co}_x\text{Zn}_{0.4}\text{Fe}_2\text{O}_4$  ferrites

a peaking nature ( $Z''_{\max}$ ) which shifts to lower frequencies with increasing Co content, indicating the presence of a relaxation phenomenon in the prepared samples. This is in good agreement with the results found in the electrical modulus section.

Figure 9 depicts the Nyquist plots ( $Z''$  vs.  $Z'$ ) at RT for  $\text{Mg}_{0.6-x}\text{Co}_x\text{Zn}_{0.4}\text{Fe}_2\text{O}_4$  ferrites. As obvious from this figure, the spectra show semicircles and arcs whose maxima and diameters increase with increasing Co content. The analysis of such plots makes it possible to separate the contribution of grains and grain boundaries in the transport mechanism in the samples. This separation is achieved by an adjustment of the Nyquist plots by an appropriate equivalent circuit. Generally, the complex ferrite systems do not always behave like ideal simple elements in impedance. For this reason, many electrical circuits are presented and interpreted in the literature to model the impedance data and represent physically the various charge migrations and polarization phenomena occurring in the materials [20, 41–45]. To explain the electrical behavior of the prepared ferrites, the impedance data are fitted using two parallel combinations of resistance and constant phase element in series. The configuration of this circuit is of the type of  $(R_g//CPE_g + R_{gb}//CPE_{gb})$  as shown in the inset of Fig. 9, where  $R_g$ ,  $R_{gb}$ ,  $CPE_g$ , and  $CPE_{gb}$  are the resistances and constant phase elements of two electroactive regions, i.e., grain boundary and grain, respectively. The impedance response of a constant phase element (CPE) can be defined as [42]

$$Z_{CPE} = \frac{1}{Q(j\omega)^\alpha} \quad (16)$$

Here,  $Q$  and  $\alpha$  are the CPE parameters which are frequency independent. The parameter  $\alpha$  represents an angle of

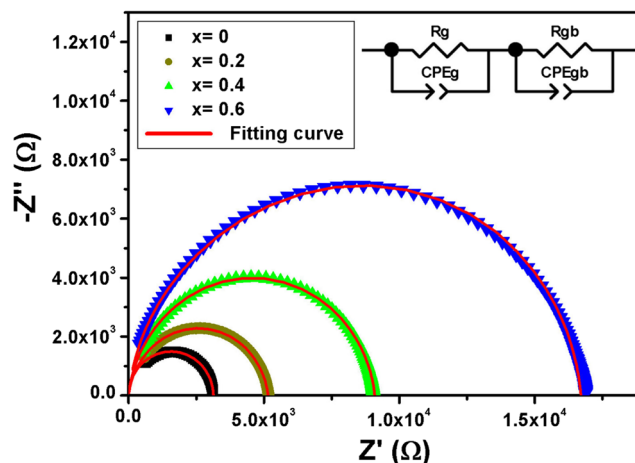


**Fig. 9** Nyquist plots of  $\text{Mg}_{0.6-x}\text{Co}_x\text{Zn}_{0.4}\text{Fe}_2\text{O}_4$  ferrites at RT. Inset: the appropriate electrical equivalent circuit used for modeling the impedance spectra



**Table 4** Electrical parameters of equivalent circuit deduced from Nyquist plots at RT for  $\text{Mg}_{0.6-x}\text{Co}_x\text{Zn}_{0.4}\text{Fe}_2\text{O}_4$  ferrites

$x$	Grain			Grain boundary		
	$R_g$ ( $\Omega$ )	$Q \times 10^{-9}$ (F)	$\alpha$	$R_{gb}$ ( $\Omega$ )	$Q \times 10^{-9}$ (F)	$\alpha$
0	790	1.7	0.994	2338	1.09	0.987
0.2	1996	16.6	0.915	3153	8.93	0.930
0.4	3100	12.0	0.920	5991	8.10	0.932
0.6	4700	1.1	0.925	11998	0.80	0.948

rotation in the complex plane with respect to the impedance response of an ideal capacitor, and it always ranges between 0.5 and 1. The CPE coefficient  $Q$  is the combination of properties related to both the surface and the electroactive species, and represents the differential capacitance of the interface when  $\alpha$  is 1. To determine the parameters of the equivalent circuit corresponding to each sample, we carried out the modeling of the impedance spectra using *Zview* software [46]. As shown in Fig. 9, the good agreement between the experimental spectra and the calculated curves shows that the proposed equivalent circuit describes well the electrical behavior of the samples. The values of all fitted parameters obtained for each sample are summarized in Table 4. The obtained  $R_g$  and  $R_{gb}$  values increase with increasing Co content which indicates a decrease of the conductivity as a function of cobalt substitution. Besides, the values of  $R_{gb}$  are larger compared to  $R_g$  values. This means that the resistances of these ferrites resulted mostly from the grain boundary effect.

## 4 Conclusion

The effect of Co doping on microstructural, infrared, and electrical properties of  $\text{Mg}_{0.6-x}\text{Co}_x\text{Zn}_{0.4}\text{Fe}_2\text{O}_4$  ferrites prepared using the sol–gel method has been investigated in this work. Analysis of XRD results shows the cubic spinel structure of the prepared samples. Only tetrahedral stretching peaks are clearly observed from FTIR spectra. Conductivity is found to decrease, due to the increase of the porosity with Co doping. The decrease in dielectric constants with frequency for the samples is due to the decrease in the polarization. Variations of imaginary parts of modulus and impedance show the presence of an electrical relaxation phenomenon with non-Debye type in our ferrites. From Nyquist plots, we found that the resistances of these ferrites resulted from the grain boundary effect.

## References

- Meng, Y.Y., Liu, Z.W., Dai, H.C., Yu, H.Y., Zeng, D.C., Shukla, S., et al.: Powder Technol. **229**, 270 (2012)
- Idrees, M., Nadeem, M., Hassan, M.M.: J. Phys. D. Appl. Phys. **43**, 155401 (2010)
- Rahman, M.A., Hossain, A.K.M.A.: Phys. Scr. **89**, 025803 (2014)
- Selmi, A., Hcini, S., Rahmouni, H., Omri, A., Bouazizi, M.L., Dhahri, A.: Phase Transit. **90**, 942 (2017)
- Oumezzine, E., Hcini, S., Rhouma, F.I.H., Oumezzine, M.: J. Alloys Compd. **726**, 187 (2017)
- Jemaï, R., Lahouli, R., Hcini, S., Rahmouni, H., Khirouni, K.: J. Alloys Compd. **705**, 340 (2017)
- Hajarpour, S., Gheisari, Kh., Honarbakhsh Raouf, A.: J. Magn. Magn. Mater. **329**, 165 (2013)
- Raghuvanshi, S., Mazaleyrat, F., Kane, S.N.: AIP Adv. **8**, 047804 (2018)
- Mohammed, K.A., Al-Rawas, A.D., Gismelseed, A.M., Sellai, A., Widatallah, H.M., Yousif, A., Elzain, M.E., Shongwe, M.: Physica B **407**, 795 (2012)
- Kassabova-Zhetcheva, V.D., Pavlova, L.P., Samuneva, B.I., Cherkezova-Zheleva, Z.P., Mitov, I.G., Mikhov, M.T.: Cent. Eur. J. Chem. **5**(1), 107 (2007)
- Mazen, S.A., Mansour, S.F., Zaki, H.M.: Cryst. Res. Technol. **38**, 471 (2003)
- Bobade, D.H., Rathod, S.M., Mane, M.L.: Physica B **407**, 3700 (2012)
- Rafiq, M.A., Khan, M.A., Asghar, M., Ilyas, S.Z., Shakir, I., Shahid, M., Warsi, M.F.: Ceram. Int. **10501** (2015)
- Ladgaonkar, B.P., Kolekar, C.B., Vaingankar, A.S.: Bull. Mater. Sci. **25**, 351 (2002)
- Zaki, H.M., Al-Heniti, S., Elmosalami, T.A.: J. Alloys Compd. **633**, 104 (2015)
- Oumezzine, E., Hcini, S., Baazaoui, M., Hlil, E.K., Oumezzine, M.: Powder Technol. **278**, 189 (2015)
- Shannon, R.D.: Acta Crystallogr. A **32**, 751 (1976)
- Sharma, J., Sharma, N., Parashar, J., Saxena, V.K., Bhatnagar, D., Sharma, K.B.: J. Alloys Compd. **649**, 362 (2015)
- Ahmad, Z., Atiq, S., Abbas, S.K., Ramay, S.M., Riaz, S., Naseem, S.: Ceram. Int. **42**, 18271 (2016)
- Batoo, K.M., Kumar, S., Lee, C.G., Alimuddin: Curr. Appl. Phys. **9**, 826 (2009)
- Ahmed, M.A., Afify, H.H., El Zawawia, I.K., Azab, A.A.: J. Magn. Magn. Mater. **324**, 2199 (2012)
- Khot, V.M., Salunkhe, A.B., Phadatar, M.R., Pawar, S.H.: Chem. Phys. **132**, 782 (2012)
- Druca, A.C., Borhana, A.I., Diaconu, A., Iordana, A.R., Nedelcub, G.G., Leontieb, L., Palamaru, M.N.: Ceram. Int. **40**, 13573 (2017)
- Mund, H.S., Ahuja, B.L.: Mater. Res. Bull. **85**, 228 (2017)
- Ortega, N., Kumar, A., Bhattacharya, P., Majumder, S.B., Katiyar, R.S.: Phys. Rev. B **77**, 014111 (2008)
- El-Hiti, M.A.: J. Phys. D Appl. Phys. **29**, 501 (1996)
- Anis-ur-Rehman, M., Malik, M.A., Khan, K., Maqsood, A.: J. Nanopart. Res. **14**, 1 (2011)
- Shaikh, P.A., Kambale, R.C., Rao, A.V., Kolekar, Y.D.: J. Alloys Compd. **482**, 276 (2009)
- Atiq, S., Majeed, M., Ahmad, A., Abbas, S.K., Saleem, M., Riaz, S., Naseem, S.: J. Magn. Magn. Mater. **43**, 2486 (2017)

30. Chakrabarty, S., Pal, M., Dutta, A.: *Mater. Chem. Phys.* **153**, 221 (2015)
31. Dhaou, M.H., Hcini, S., Mallah, A., Bouazizi, M.L., Jemni, A.: *Appl. Phys. A* **123**, 8 (2017)
32. Hcini, S., Omri, A., Boudard, M., Bouazizi, M.L., Dhahri, A., Touileb, K.: *J. Mater. Sci. Mater. Electron.* **29**, 6879 (2018)
33. Maxwell, J.C.: *Electricity and Magnetism*. Oxford University Press, London (1973)
34. Jadhav, P.A., Devan, R.S., Kolekar, Y.D., Chougule, B.K.: *J. Phys. Chem. Solids* **70**, 396 (2009)
35. Vasoya, N.H., Jha, P.K., Saija, K.G., Dolia, S.N., Zankat, K.B., Modi, K.B.: *J. Electron. Mater.* **45**, 917 (2016)
36. Saha, S., Sinha, T.P.: *Phys. Rev. B* **65**, 1341 (2005)
37. Padmasree, K.P., Kanchan, D.D., Kulkarni, A.R.: *Solid State Ion.* **177**, 475 (2006)
38. Bergman, R.: *J. Appl. Phys.* **88**, 1356 (2000)
39. Rao, K.S., Krishna, P.M., Prasad, D.M., Gangadharudu, D.: *J. Mater. Sci.* **42**, 4801 (2007)
40. Sivakumar, N., Narayanasamy, A., Ponpandian, N., Govindaraj, G.: *J. Appl. Phys.* **101**, 084116 (2007)
41. Batoor, K.M.: *Physica B* **406**, 382 (2011)
42. Guo, J., Zhang, H., He, Z., Li, S., Li, Z.: *J. Mater. Sci. Mater. Electron.* **29**, 2491 (2018)
43. Naz, S., Durrani, S.K., Mehmood, M., Nadeem, M., Khan, A.A.: *J. Therm. Anal. Calorim.* **126**, 381 (2016)
44. Atif, M., Nadeem, M.: *J. Sol-Gel Sci. Technol.* **72**, 615 (2014)
45. Atif, M., Idrees, M., Nadeem, M., Siddiquec, M., Ashraf, W.: *RSC Adv.* **6**, 20876–20885 (2016)
46. Johnson, D.: *ZView: a Software Program for IES Analysis, Version 2.8*. Scribner Associates, Inc., Southern Pines (2008)